

MIT Open Access Articles

Chirped-pulse millimeter-wave spectroscopy: Spectrum, dynamics, and manipulation of Rydberg–Rydberg transitions

The MIT Faculty has made this article openly available. **Please share** how this access benefits you. Your story matters.

Citation: Colombo, Anthony P., Yan Zhou, Kirill Prozument, Stephen L. Coy, and Robert W. Field. "Chirped-pulse millimeter-wave spectroscopy: Spectrum, dynamics, and manipulation of Rydberg–Rydberg transitions." *The Journal of Chemical Physics* 138, no. 1 (2013): 014301. © 2013 American Institute of Physics.

As Published: <http://dx.doi.org/10.1063/1.4772762>

Publisher: American Institute of Physics

Persistent URL: <http://hdl.handle.net/1721.1/83624>

Version: Final published version: final published article, as it appeared in a journal, conference proceedings, or other formally published context

Terms of Use: Article is made available in accordance with the publisher's policy and may be subject to US copyright law. Please refer to the publisher's site for terms of use.



Chirped-pulse millimeter-wave spectroscopy: Spectrum, dynamics, and manipulation of Rydberg–Rydberg transitions

Anthony P. Colombo, Yan Zhou, Kirill Prozument, Stephen L. Coy, and Robert W. Field

Citation: *The Journal of Chemical Physics* **138**, 014301 (2013); doi: 10.1063/1.4772762

View online: <http://dx.doi.org/10.1063/1.4772762>

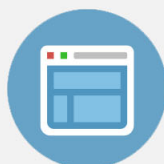
View Table of Contents: <http://scitation.aip.org/content/aip/journal/jcp/138/1?ver=pdfcov>

Published by the [AIP Publishing](#)



Re-register for Table of Content Alerts

Create a profile.



Sign up today!



Chirped-pulse millimeter-wave spectroscopy: Spectrum, dynamics, and manipulation of Rydberg–Rydberg transitions

Anthony P. Colombo, Yan Zhou, Kirill Prozument, Stephen L. Coy, and Robert W. Field^{a)}
 Department of Chemistry, Massachusetts Institute of Technology, Cambridge, Massachusetts 02139, USA

(Received 3 October 2012; accepted 6 December 2012; published online 2 January 2013)

We apply the chirped-pulse millimeter-wave (CPmmW) technique to transitions between Rydberg states in calcium atoms. The unique feature of Rydberg–Rydberg transitions is that they have enormous electric dipole transition moments (~ 5 kiloDebye at $n^* \sim 40$, where n^* is the effective principal quantum number), so they interact strongly with the mm-wave radiation. After polarization by a mm-wave pulse in the 70–84 GHz frequency region, the excited transitions re-radiate free induction decay (FID) at their resonant frequencies, and the FID is heterodyne-detected by the CPmmW spectrometer. Data collection and averaging are performed in the time domain. The spectral resolution is ~ 100 kHz. Because of the large transition dipole moments, the available mm-wave power is sufficient to polarize the entire bandwidth of the spectrometer (12 GHz) in each pulse, and high-resolution survey spectra may be collected. Both absorptive and emissive transitions are observed, and they are distinguished by the phase of their FID relative to that of the excitation pulse. With the combination of the large transition dipole moments and direct monitoring of transitions, we observe dynamics, such as transient nutations from the interference of the excitation pulse with the polarization that it induces in the sample. Since the waveform produced by the mm-wave source may be precisely controlled, we can populate states with high angular momentum by a sequence of pulses while recording the results of these manipulations in the time domain. We also probe the superradiant decay of the Rydberg sample using photon echoes. The application of the CPmmW technique to transitions between Rydberg states of molecules is discussed. © 2013 American Institute of Physics. [<http://dx.doi.org/10.1063/1.4772762>]

I. INTRODUCTION

Electronic transitions between Rydberg states of atoms and molecules are unique in that they may have very large electric dipole transition moments. For Rydberg–Rydberg transitions with $|\Delta n^*| \leq 1$, where n^* is the effective principal quantum number,¹ the transition dipole moment, μ , scales as the radius of the Rydberg orbital, which is proportional to $(n^*)^2$ (Ref. 2, p. 26). At $n^* \sim 40$, $|\Delta n^*| \leq 1$ Rydberg–Rydberg transition dipole moments are typically ~ 5 kiloDebye. These transition dipole moments are orders of magnitude larger than, for example, the ~ 10 D dipole moments for *maximally allowed* optical transitions in a molecule.³ Because of their large transition dipole moments, Rydberg states interact strongly with electromagnetic radiation and, via this radiation, with each other.

Millimeter-wave spectroscopy is an established tool for high-resolution studies of Rydberg atoms^{4–9} and has more recently been extended to Rydberg–Rydberg transitions in molecules.^{10–13} Millimeter-wave (and microwave) spectroscopy is a powerful method for observing the fine and hyperfine structure of Rydberg states, as well as for determining properties of the ion-core, such as its electric multipole moments and polarizabilities.¹⁴

Recently, Pate and co-workers^{15–17} developed the chirped pulse Fourier transform microwave (CP-FTMW) technique,

which has revolutionized the field of rotational spectroscopy. Instead of stepping sequentially through individual resolution elements in the frequency domain, a frequency-chirped microwave pulse polarizes a large bandwidth (~ 10 GHz) of rotational transitions in a molecular sample. All of these polarized transitions then re-radiate free induction decay (FID) at their resonant frequencies, which is heterodyne-detected directly and in a broadband fashion. In this way, the CP-FTMW method allows for the collection of spectra that are simultaneously broadband and high resolution (better than 1 MHz) in a microwave frequency region (7–18 GHz). Chirped pulse mm-wave (CPmmW) spectroscopy is an extension of CP-FTMW to the mm-wave frequency region.¹⁸ Like CP-FTMW, CPmmW provides single-shot coverage of ~ 10 GHz of spectrum at ~ 100 kHz resolution, but at frequencies of 70–102 GHz.

In this work, we discuss the application of the CPmmW technique to Rydberg–Rydberg transitions, the initial results of which are reported in Ref. 19. In the case of CPmmW rotational spectroscopy, typical transition moments are ~ 1 D, and hundreds of watts would be needed to fully polarize the molecular transitions over the entire bandwidth of the spectrometer. However, the broadband power that is presently available in the mm-wave region is severely limited. For Rydberg–Rydberg transitions with ~ 5 kD transition dipole moments, mm-wave power requirements are reduced by a factor of $\sim 10^6$, compared to a chirped pulse rotational experiment, because the power required to completely polarize a

^{a)} Author to whom correspondence should be addressed. Electronic mail: rwfield@mit.edu.

sample scales as μ^{-2} . Current mm-wave technology is well matched to this application.

The CPmmW method is a novel way to obtain spectra of Rydberg atoms and molecules. Transitions between Rydberg states have typically been detected indirectly by collecting ions, electrons, or ultraviolet photons.^{7,9,10,13,20–35} However, few studies have *directly* detected Rydberg–Rydberg transitions.³⁶ Along with spectroscopy, through the combination of direct, time-domain detection and large transition dipole moments, we observe dynamical phenomena, such as transient nutations, photon echoes, and superradiant decay. In addition, the coherent mm-wave source can be used to manipulate ensembles that possess these large transition dipole moments; the results of these manipulations are monitored with the CPmmW spectrometer.

Here, we examine CPmmW transitions in Rydberg states of the calcium atom, which serves as a convenient system for initial study. The spectroscopy of calcium is simplified by the existence of only one abundant isotope, which has zero nuclear spin. Much of the low orbital angular momentum ($\ell \leq 3$) structure of the singlet Rydberg levels in calcium is known from optical studies.^{37–41} Additionally, Gentile *et al.*⁷ used microwave and mm-wave spectroscopy to observe the singlet and triplet *S*, *P*, and *D* Rydberg series for principal quantum number $n = 22–55$. The $n = 23–25$ singlet *F* and *G* states were examined by Vaidyanathan *et al.*⁴² using microwave spectroscopy. Consequently, the transition frequencies observed in the present work were either *a priori* known to microwave precision or, because of the known quantum defects, were easily estimated well within the 12-GHz bandwidth of the CPmmW spectrometer.

II. EXPERIMENTAL METHODS

The simplest laser/mm-wave excitation schemes used in this work are depicted in Fig. 1. Two pulsed dye lasers (Lambda Physik Scanmate 2E) excite calcium atoms to an initial Rydberg state. Both dye lasers are pumped at a 20-Hz repetition rate by an injection-seeded Spectra-Physics GCR-290 Nd:YAG laser with a ~ 7 ns pulse duration. The first transition, from the ground $4s^2 \ ^1S_0$ state to the $4s5p \ ^1P_1$ state, uses 544 nm radiation doubled in a β -BBO crystal to 272 nm. The second optical transition populates either a $4sns \ ^1S_0$ or a $4snd \ ^1D_2$ level of $30 < n^* < 60$, which requires laser wavelengths around 800 nm. A chirped or Fourier-transform limited mm-wave pulse then excites Rydberg–Rydberg transitions between 70 and 84 GHz. In addition to transferring population into the target Rydberg state, the mm-wave pulse polarizes the transition between the two Rydberg states. This polarization is detected in the form of the FID signal. From a 1S_0 initial Rydberg state, only $^1S_0-^1P_1$ transitions may be observed, and from 1D_2 , $^1D_2-^1P_1$, and $^1D_2-^1F_3$ transitions are observable. The laser beams and the mm-waves are vertically polarized, so *all* of the Rydberg states sampled in these experiments are nominally $m = 0$, where m is the magnetic quantum number.

The available frequency range of our mm-wave spectrometer determines the lowest n^* at which Rydberg–Rydberg

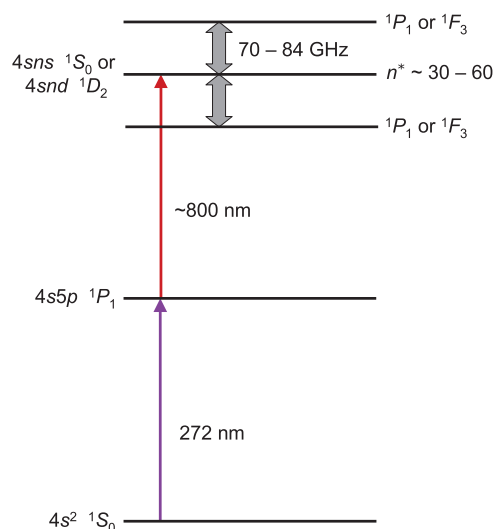


FIG. 1. Schematic of stepwise, three-photon excitations of calcium. Sequential laser pulses (thin arrows) populate a 1S_0 or 1D_2 Rydberg state with effective principal quantum number, n^* , between 30 and 60. The mm-waves (thick arrows) may then transfer population into and create coherences with levels in the 70–84 GHz frequency range. The observable types of Rydberg–Rydberg transitions are $^1S_0-^1P_1$, $^1D_2-^1P_1$, and $^1D_2-^1F_3$. Because free induction decay (FID) is detected, transitions to both higher and lower energy are observed.

transitions can be observed. The $|\Delta n^*| \leq 1$ level spacings scale as $2R/(n^*)^3$, where R is the Rydberg constant. Below $n^* \approx 30$, the states with allowed $|\Delta n^*| \leq 1$ transitions are too high-frequency for the spectrometer. At high n^* , though, $|\Delta n^*|$ for accessible transitions need not be ≤ 1 , and the available frequency range is no longer a restriction. Also, available mm-wave power is not a limitation in our experiments, so the smaller transition moments of $|\Delta n^*| > 1$ transitions do not pose a problem. However, for $n^* \gtrsim 60$, the level density becomes sufficiently high that optical transitions into multiple Rydberg states fall within the 1-GHz bandwidth of the dye laser, and we have not investigated mm-wave transitions in this n^* region.

To generate the mm-waves, a 4.2 GS/s arbitrary waveform generator (AWG, Tektronix AWG710B) first creates a user-designed pulse at 0.2–2 GHz, which is then mixed with a 10.7-GHz phase-locked oscillator (Miteq PLDRO-10-10700-3-8P). A bandpass filter transmits the lower frequency sideband (8.7–10.5 GHz) from the mixer, and the waveform is sent through an active multiplier chain that octuples the frequency and, if the pulse is chirped, the bandwidth. The multipliers generate 30 mW in the 70–84 GHz output range. A 60-dB variable attenuator is appended after the multipliers. This attenuation is necessary to prevent overdriving the Rydberg–Rydberg transitions. When additional attenuation is required, a copy of Ref. 3 is used.⁴³ A 24-dBi standard gain horn broadcasts the mm-wave radiation, which is collimated by Teflon lenses before entering the CPmmW vacuum chamber. After interacting with the calcium sample ($\sim 10^5$ Rydberg atoms/cm³), Teflon lenses focus the mm-waves into another gain horn for collection. Radiation is then heterodyne-detected with a W-band Gunn oscillator (J. E. Carlstrom Co. H129), which is locked to a harmonic of

the 10.7-GHz oscillator. The down-converted, low-frequency signal is then recorded directly on a 12.5-GHz oscilloscope (Tektronix DPO71254B, 50 GS/s). The 12.5-GHz bandwidth of the oscilloscope restricts the bandwidth within the 70–84 GHz region that can be collected in a single chirp. The oscilloscope and all of the frequency-generating components are phase locked to a 10-MHz rubidium frequency standard (Stanford Research Systems FS725), which allows the mm-wave signals (transmitted radiation and FID) to be phase-coherently averaged in the time domain. The resolution of the acquired spectra is ~ 100 kHz, which is determined by the duration of the collected FID (typically ~ 10 μ s). The CPmmW spectrometer is described in detail in Ref. 18.

When rotational transitions are observed by the CPmmW spectrometer in a supersonic jet expansion,¹⁸ the number density of molecules that may be polarized by the mm-waves (the number density difference per quantum state) is typically $\sim 10^{11}$ molecules/cm³. However, such a high number density of Rydberg atoms would encounter signal loss via dipole-dipole collisional dephasing^{30,34,44–49} and cooperative effects such as superradiant decay.^{5,19,32,50–55} Therefore, we enlarged the interaction volume to compensate for the required lower density of emitters. A schematic of the experiment is shown in Fig. 2. Calcium atoms are produced by ablation of a calcium rod with 5 mJ of the third harmonic of a Spectra-Physics GCR-130 Nd:YAG laser, which is focused to a ≈ 300 μ m spot.

The ablated calcium is entrained in a pulse of helium or argon gas, which supersonically expands from a 20-psi stagnation pressure into the CPmmW chamber. The center of the region where the lasers, mm-waves, and beam of calcium atoms intersect is about 12 cm downstream from the 0.5-mm diameter nozzle. At this distance, the jet has expanded so that its cross-sectional area matches that of the mm-waves (~ 10 cm²), which are not tightly focused. Before entering the CPmmW chamber through a fused silica window, the mm-waves are reflected off of an aluminum mirror. This mirror has a 12-mm hole in its center, and a diverging lens is placed immediately before the hole so that the laser and mm-wave beams have similar diameters in the interaction region. The dye laser beam profiles cover approximately 6 cm², and the total interaction volume is about 50 cm³. Helmholtz coils compensate for ambient magnetic fields that split the Rydberg–Rydberg transitions and/or broaden the lineshapes.

In order to determine the correct laser wavelengths for the CPmmW experiments, we also detect laser transitions into calcium Rydberg states by pulsed-field ionization (PFI) in the same apparatus—but in a different chamber. To reach the ionization region, the calcium jet travels past the mm-wave-illuminated volume to a 1-mm skimmer, which is 40 cm away from the nozzle and which separates the CPmmW chamber from the PFI chamber. After traversing the skimmer, the jet propagates another 25 cm to the ionization region. The PFI

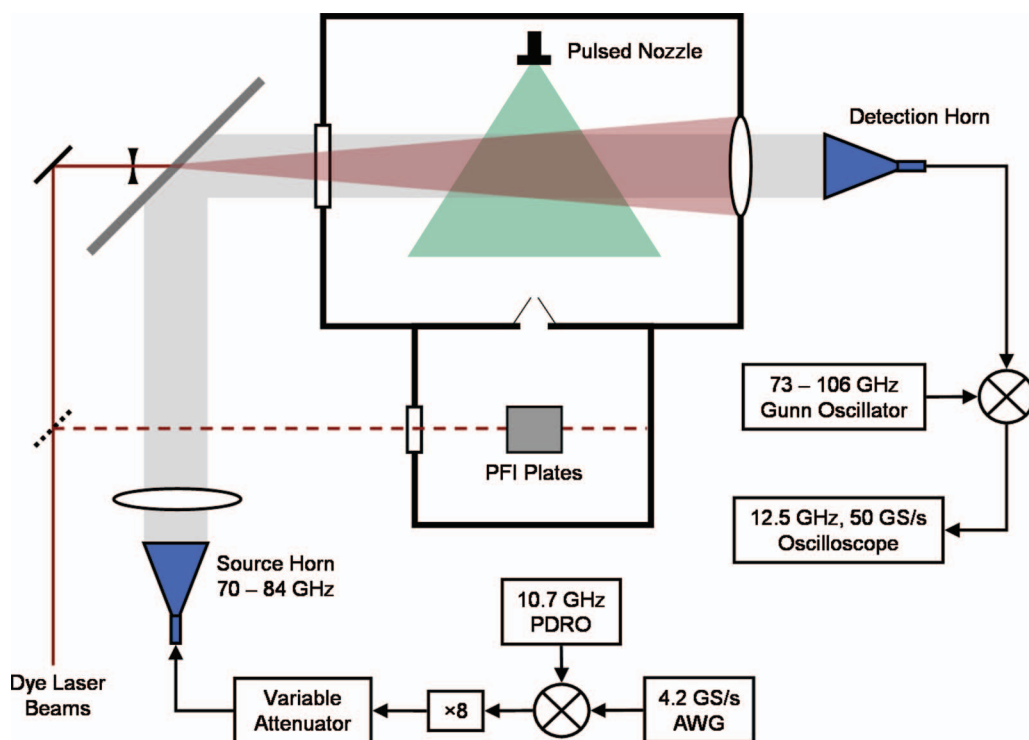


FIG. 2. Diagram of the experimental apparatus for observing Rydberg–Rydberg transitions. The laser beams pass through an expanding lens and an aperture in a metal mirror before they excite calcium atoms from the ablation source (not shown) into the initial Rydberg state. The mm-waves (shaded gray) are generated by mixing the output of the arbitrary waveform generator (AWG) with a phase-locked dielectric resonant oscillator (PDRO) and octupling the resulting waveform. A gain horn broadcasts the mm-waves, which then interact with the excited calcium atom sample. Another horn collects both transmitted radiation and free induction decay (FID). Teflon lenses collimate/focus the radiation before and after the interaction region. Detected mm-waves are down-converted by mixing with radiation from a W-band Gunn oscillator, and the resulting signal, between dc and 12.5 GHz, is sent to a fast oscilloscope. Each of the mm-wave generation and detection components is phase-locked to a 10-MHz frequency standard (not shown), which enables averaging in the time domain. The lasers may also be directed into the pulsed field ionization (PFI) region (broken-line path), before which the supersonic expansion is skimmed. The PFI setup is used to tune the lasers into resonance with selected transitions.

TABLE I. Quantum numbers of transitions discussed in this work are listed in both $n^*\ell$ and $n\ell$ notation.

$n^*\ell$	$n\ell$
34.13p–33.67s	36p–36s
41.73d–40.88f	43d–41f
55.8d–53.9f	57d–54f
55.9g–53.9f	56g–54f
55.9g–54.0h	56g–54h

instrument (as well as the ablation source) is described in detail in Ref. 29. When the first laser is tuned to resonance with the $4s5p\ ^1P_1 \leftarrow 4s^2\ ^1S_0$ transition, $1+1'$ resonance enhanced multiphoton ionization may be observed. A two-color PFI signal is used to tune the 800-nm laser to resonance with transitions from the $4s5p\ ^1P_1$ state into selected Rydberg states. It is necessary to detect PFI in a separate chamber because the PFI components generate electric fields that shift and broaden the mm-wave transitions. Conversion of the apparatus between the CPmmW and PFI experiments requires only a change in the delay for the dye laser pulses and adjustment of two mirrors, a process which is accomplished in a few minutes.

III. RESULTS

A. Excitation methods and Rydberg–Rydberg FID spectra

Each Rydberg state in a transition is denoted by $n^*\ell$.⁵⁶ For reference, Table I contains both the $n^*\ell$ and $n\ell$ labels of all transitions discussed in this work. We excite Rydberg–Rydberg transitions in two ways, examples of which are shown in Fig. 3. In both cases, lasers initially populate the

$33.67s$ state in calcium, and the mm-waves then probe the $34.13p$ – $33.67s$ transition. In Fig. 3(a), the AWG is set to a single frequency, and the bandwidth of the excitation pulse is Fourier-transform-limited. The $34.13p$ – $33.67s$ transition has a calculated electric dipole transition moment¹⁹ of 3439 D, and $\pi/2$ polarization occurs in 10 ns with $2\ \mu\text{W}$ of power spread over an $\approx 6\ \text{cm}^2$ spot. Here, the large Rydberg–Rydberg transition dipole moment makes it possible for a relatively short pulse to optimally polarize the transition. Alternatively, a resonant, 500-ns pulse would achieve $\pi/2$ polarization for the same transition at 0.6 nW, since the power required for a given pulse area scales as Δt^{-2} , where Δt is the pulse duration.

In Fig. 3(c), the frequency of the excitation pulse is chirped linearly in time, and the frequency range of the chirp, rather than the duration of the pulse, determines the bandwidth of the pulse. Since the power of a chirped pulse is distributed over more bandwidth than a transform-limited pulse, a combination of higher power and/or longer pulse duration is required to generate a $\pi/2$ flip angle. For example, the chirp in Fig. 3(c) has a bandwidth of 500 MHz and a duration of $0.5\ \mu\text{s}$, which requires $0.2\ \mu\text{W}$ for optimum polarization of the $34.13p$ – $33.67s$ transition. To achieve a given flip angle, the power needed for a chirped pulse scales linearly with the bandwidth if Δt is fixed or scales as Δt^{-1} if the bandwidth is fixed.⁵⁷ Of course, for both single-frequency and chirped excitations, the use of shorter pulses (with more power) maximizes the total signal because the earliest, most intense part of the FID cannot be collected while the excitation pulse is present.

The spectra in Fig. 3 have S/N ratios of about 700 and were obtained from 5000 averages, which required approximately 5 min to accumulate. About 0.5 mJ of power were used for each laser pulse, and we estimate that the number density of Rydberg atoms in

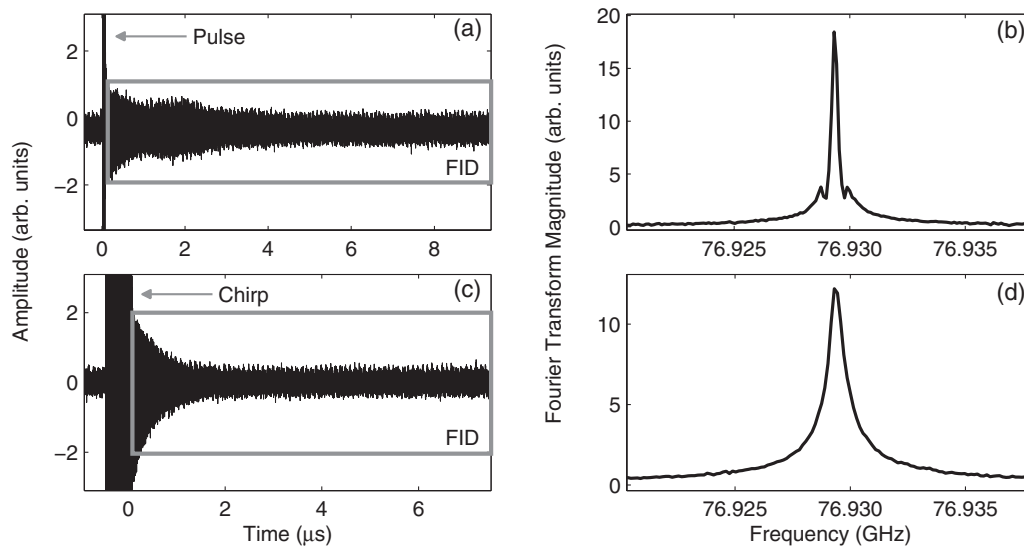


FIG. 3. Basic single-frequency and chirped excitations of the $34.13p$ – $33.67s$ transition in Ca. (a) A 10-ns, transform-limited pulse (with amplitude far larger than the vertical scale of the figure) is followed by FID from calcium in an argon jet expansion. The pulse is centered at the 76.9293 GHz transition frequency.⁷ (b) The magnitude Fourier transform of the FID exhibits Zeeman splittings caused by the stray magnetic field that is not completely cancelled by the Helmholtz coils. The full width at half maximum of the center feature is 420 kHz. (c) A chirp over 500 MHz in $0.5\ \mu\text{s}$ excites the same transition in a helium expansion. (d) The Doppler width, which is larger for a helium beam because helium is less massive than argon, is similar to the magnetic field splitting. Therefore, the Zeeman components are not resolved. Both time traces contain artifact oscillations because the 10 MHz frequency from the rubidium standard is present in the detection arm of the spectrometer.

a single n^* , ℓ , $m = 0$ quantum state is $\sim 10^5/\text{cm}^3$.¹⁹ The usable FID persists for approximately 10 μs , well after the signal has fallen below the noise floor visible in the time trace. Linewidths are on the order of 500 kHz, which is consistent with the Doppler dephasing calculated for the geometry of our unskimmed jet expansion plus residual stray magnetic fields. The linewidths are similar in magnitude to those observed in Ref. 7, where the broadening had a different cause: the transit time of the Rydberg sample in a skimmed jet expansion. In cases where the same transition is measured, the frequencies agree with those in Ref. 7 within experimental uncertainty, which is ~ 10 kHz in Ref. 7 and ~ 1 kHz here. In Fig. 3, the S/N ratio at 5000 averages suggests that a single shot would have S/N of around 10, and experimentally, single-shot signal is clearly visible. We estimate that the smallest number density that we can detect (S/N ratio = 3) with 5000 averages is approximately 4×10^3 Rydberg emitters/ cm^3 , or, in our experimental geometry, $\lesssim 2 \times 10^5$ total Rydberg atoms.

B. Transient nutations and transition phases

One consequence of the kiloDebye dipole moments of Rydberg–Rydberg transitions is that the sample polarization induced by the excitation pulse can be comparable to that of the excitation pulse itself. Under such conditions, the emission from the sample polarization combines coherently with the excitation pulse while the pulse is present, resulting in transient nutations.^{19,58,59} After the excitation pulse has ended, the sample polarization continues to emit radiation, which is then in the form of FID. Examples of transient nutations are shown in Fig. 4 for single-frequency, nearly- $\pi/2$ excitations of the $34.13p$ – $33.67s$ and $41.73d$ – $40.88f$ transitions. In Fig. 4(a), the power used for the $34.13p$ – $33.67s$ transition is 0.3 nW at 76.9293 GHz for 0.5 μs . The $34.13p$ – $33.67s$ transition is absorptive, since the lower energy state is initially populated. During the mm-wave pulse, the sample emission interferes destructively with the excitation pulse as the sample accrues polarization, and the amplitude of the excitation pulse appears to decrease in the time domain—consistent with energy conservation. Conversely, Fig. 4(b) illustrates an emissive (downward) transition, in which the lasers populate $41.73d$. The $41.73d$ – $40.88f$ transition is resonantly excited for 0.2 μs with 1 nW at 79.1212 GHz. Here, the amplitude of the excitation pulse appears to increase with time because the emission from the sample polarization interferes constructively with the pulse. In this way, the nutations immediately display whether the transition is upward or downward in energy relative to the initial population. Transient nutations are also observed during chirped excitation.¹⁹

In Fig. 4(a), the excitation pulse and the sample emission are π radians out of phase (absorptive), whereas in Fig. 4(b) they have the same phase (emissive). However, the phase difference between the excitation pulse and the FID can also be extracted from the oscillations that are recorded directly in the time domain. To estimate the precision with which the phase of any FID, ϕ_{FID} , can be determined, we assume that the uncertainty in the time measurement, which comes from the 10-MHz frequency standard, is negligible.

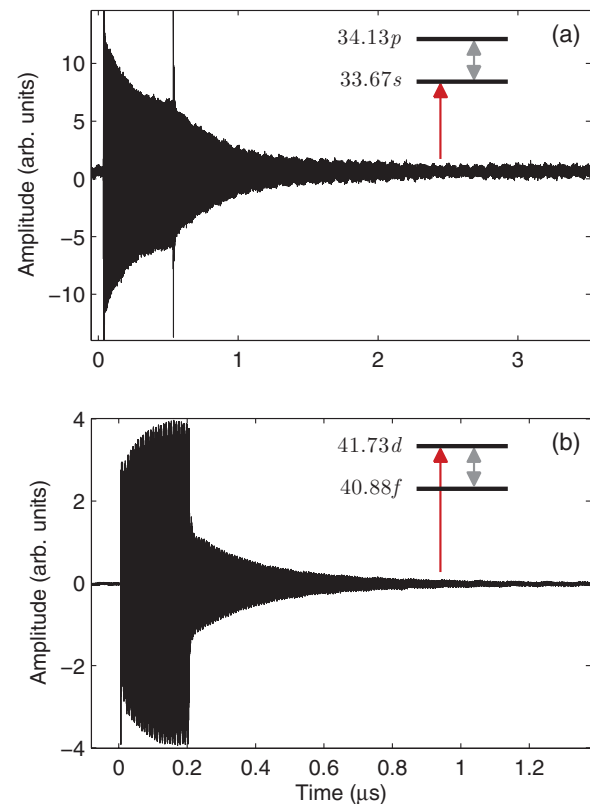


FIG. 4. Transient nutations display the absorptive or emissive nature of transitions. (a) In the time trace for the absorptive $34.13p$ – $33.67s$ transition, the excitation pulse is π radians out of phase with emission from the polarization of the Rydberg sample that the pulse generates. The resulting destructive interference is responsible for the appearance of the decreasing amplitude during the excitation pulse. After the excitation pulse ends at around 0.5 μs , the sample polarization continues to emit radiation, but as FID. The inset shows the level diagram, where the laser (red, single arrow) initially populates the lower $33.67s$ state, and the mm-waves (gray arrows) create a coherence with the higher energy $34.13p$ state. (b) The $41.73d$ – $40.88f$ transition is emissive. The sample polarization emission interferes constructively with the excitation pulse, the amplitude of which appears to increase until 0.2 μs , when the excitation pulse terminates. In this excitation sequence, the laser transfers population into the upper state, and the mm-wave transition to the $40.88f$ state is downward in energy.

We also assume that the relative standard deviation (RSD) of ϕ_{FID} is no smaller than the combination of relative uncertainties in the other fitted parameters (decay rate, γ , frequency, ν , and amplitude, A) that reproduce the FID. That is, we assume that $\text{RSD}_{\phi}^2 = \text{RSD}_{\gamma}^2 + \text{RSD}_{\nu}^2 + \text{RSD}_A^2$ for the FID. In our experiment, the precisions of γ and A are similar (while the precision of ν is much higher), and the relative uncertainties of each are $\approx (\text{S/N ratio})^{-1}$.^{60,61} For spectra such as those in Fig. 3, the relative uncertainty in γ and A is thus $\sim 10^{-3}$, which corresponds to an uncertainty in ϕ_{FID} of $< 0.01\pi$ radians. Even this conservative estimate of the precision of the fitted ϕ_{FID} far exceeds what is necessary to distinguish absorptive (π phase difference) from emissive (0 phase difference) transitions.

For a resonant, single-frequency excitation pulse ($\omega_{\text{pulse}} = \omega_{\text{FID}}$, where ω is the angular frequency) with phase ϕ_{pulse} , the relative phase of the pulse and FID is simply $\phi_{\text{FID}} - \phi_{\text{pulse}}$. The phase of the time-domain oscillations of the excitation pulse is directly compared to the phase of the FID

oscillations, and the phase difference (π or 0) identifies the upward or downward nature of the transition. Hence, determination of the relative phase of the pulse and the FID need not require observation of nutations. Moreover, whether a transition is absorptive or emissive can be inferred from a time trace in which the excitation pulse is at a constant (possibly off-scale) amplitude. An example of this case is in Fig. 3(a), where the phase of the FID is indeed measured to be π radians different than the phase of the excitation pulse, as is expected when the lasers initially populate the lower state.

Measurement of the phase of the FID relative to that of the excitation can be extended to the case of a chirped excitation pulse. For a linearly chirped pulse, the phase at time t is

$$\phi_c(t) = \phi_0 + \omega_0 t + \frac{1}{2} \frac{\Delta\omega}{\Delta t} t^2, \quad (1)$$

where ϕ_0 is the initial phase of the chirp, ω_0 is the initial angular frequency of the chirp, and $|\Delta\omega|$ is the bandwidth of the chirp. (If the frequency of the chirp is increasing during the pulse, $\Delta\omega > 0$, and $\Delta\omega < 0$ if the frequency is decreasing.) The sweep rate of the chirp is $\Delta\omega/\Delta t$, and the frequency of the chirp at a given time is

$$\omega_c(t) = \omega_0 + \frac{\Delta\omega}{\Delta t} t. \quad (2)$$

The phase of the chirp may also be related to the instantaneous frequency by combining Eq. (1) with Eq. (2) and eliminating t ,

$$\phi_c(\omega_c) = \phi_0 + \frac{1}{2} (\omega_c^2 - \omega_0^2) \left(\frac{\Delta\omega}{\Delta t} \right)^{-1}. \quad (3)$$

If the FID of a transition is recorded at a frequency ω_{FID} and with a phase ϕ_{FID} , then the FID phase can be measured against the phase of the chirp when the chirp reaches the transition frequency.⁶² In other words, $\phi_{\text{FID}} - \phi_c(\omega_{\text{FID}})$ may be evaluated using ω_{FID} in Eq. (3). In this way, a measurement of a chirped pulse and the subsequent FID can also be used to determine whether a transition is absorptive or emissive. For example, the FID in Fig. 3(c) is determined to be π radians out of phase with the chirp when it sweeps through resonance, which is consistent with an absorptive transition.

In the case where a chirped pulse excites multiple transitions that have different values of ω_{FID} and ϕ_{FID} , the approach described here may still be employed. As long as a transition in the frequency spectrum is resolved enough that ω_{FID} and ϕ_{FID} can be determined, then each relative phase can be evaluated individually using Eq. (3).

C. Manipulations and superradiant decay

Along with the large transition dipole moments, the easily controlled, phase coherent mm-wave source allows for manipulation of Rydberg states. For example, we populate the $54.0h$ state by a sequence of three pulses, as shown in Fig. 5. The $55.8d$ state is initially populated by the laser radiation. Subsequent mm-wave pulses of 77.5720 GHz, 82.0725 GHz, and 78.8625 GHz each transfer some of the population into $53.9f$, $55.9g$, and $54.0h$, respectively. Because no pulse in the excitation sequence caused an integer multiple of π polar-

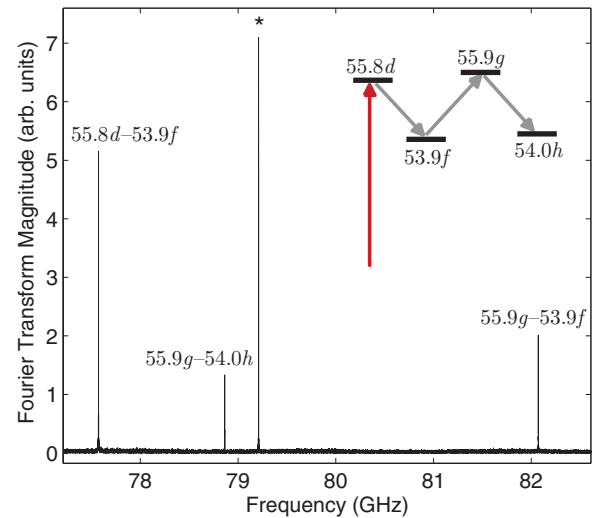


FIG. 5. One spectrum contains each $\ell \rightarrow \ell + 1$ excitation step in the multiple-component-pulse population of the $54.0h$ state. The inset shows a schematic of the four energy levels and three transitions that contribute to the spectrum. The $55.8d$ state is initially populated by the lasers (long, red arrow). Sequential, resonant mm-wave pulses (gray arrows) then excite the $55.8d$ - $53.9f$ transition at 77.5720 GHz, the $55.9g$ - $53.9f$ transition at 82.0725 GHz, and the $55.9g$ - $54.0h$ transition at 78.8625 GHz. Since no pulse area is chosen to be an integer multiple of π , each transition appears in the frequency spectrum. A known artifact (marked with an asterisk) is due to the fixed-frequency 3.96-GHz oscillator of the mm-wave spectrometer.

ization, at each step there is both FID signal and population transfer. Thus, each mm-wave transition in the $\ell \rightarrow \ell + 1 \rightarrow \ell + 2$ transition sequence appears in a single spectrum.

In addition to populating states of high angular momentum, we have observed photon echoes of the $34.13p$ - $33.67s$ transition, one of which is shown in Fig. 6. Initially a 10-ns, single-frequency pulse with 2 μW of power $\pi/2$ -polarizes the transition. The resulting FID decays (mostly) inhomogeneously due to Doppler and Zeeman broadening. After a waiting time τ , a π pulse—the same power as the $\pi/2$ pulse but twice the duration—is applied. The π pulse reverses the

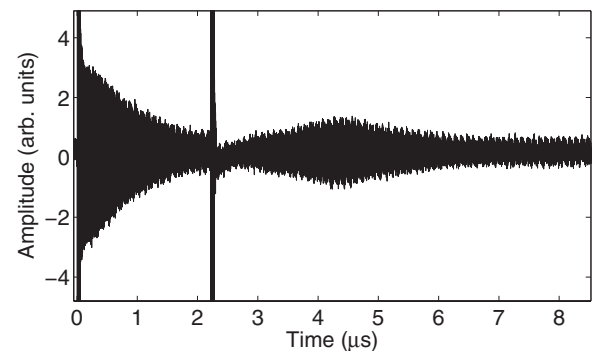


FIG. 6. Rydberg mm-wave photon echo. A 10-ns $\pi/2$ pulse initially polarizes the $34.13p$ - $33.67s$ transition, and most of the dephasing of the FID is inhomogeneous. At 2.2 μs , a 20-ns π pulse is applied, which reverses the inhomogeneous dephasing. After another 2.2 μs , a fraction of the FID recovers. The decrease of the echo amplitude (relative to the initial FID) is determined primarily by the superradiant decay rate^{19,50-52,55} of this system. The dip in the signal immediately after the π pulse ends is due to the pulse saturating the amplifier in the detection arm of the spectrometer. Fine modulation is an artifact that arises from the 10-MHz phase reference in the frequency down-conversion step.

inhomogeneous components of the phase evolution, and during another period of length τ , the FID revives (incompletely), then dephases again. A time series of photon echoes of the same transition is shown in Fig. 7 for τ values of 2.0, 2.4, and 2.8 μs . The measured phase difference between each echo and initial FID is π radians, which is consistent with the π pulse inverting the two-level system. The amplitude of the echo is determined by the extent of the homogeneous decay over the $\sim 2\tau$ interval. If the homogeneous decay rate were negligible (that is, if the decay of the FID were completely inhomogeneous), then the amplitude of the echo would be equal to that of the initial FID. Conversely, in the case of a purely homogeneous decay, there would be no rephasing at all. Assuming an exponential decay of the echo amplitude relative to the FID amplitude, the homogeneous decay constant of the echoes was determined to be $4.6 \pm 0.5 \mu\text{s}$. The possible sources of homogeneous decay in our experiment are transit time of the jet expansion, blackbody radiation from the surrounding apparatus, collisional dephasing from the dipole–dipole interaction, and cooperative radiation of the Rydberg emitters (superradiance).

In our apparatus, the field of view of the detection horn is 12 cm wide, and we estimate that the average time of flight from the center of the interaction volume is about 33 μs . Thus, the transit time of the calcium emitters does not contribute significantly to the homogeneous decay.

In the case of blackbody radiation, homogeneous decay occurs in two ways: (1) the blackbody field incoherently excites the observed transition, directly causing dephasing, and (2) the field moves population into other states, decreasing the observed transition amplitude. For mechanism (1), the direct dephasing rate of a given transition by blackbody radiation is (Ref. 2, pp. 53–54)

$$\gamma_{\text{bb},1} = \frac{4\pi kT}{3\epsilon_0 c^3} \left(\frac{\mu\nu}{\hbar} \right)^2, \quad (4)$$

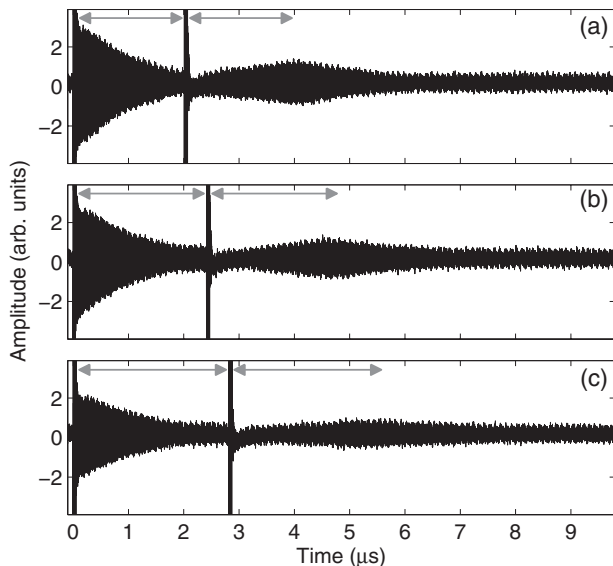


FIG. 7. Photon echoes are observed at a series of delay times. Photon echoes of the 34.13p–33.67s transition are collected with waiting times, τ , of (a) 2.0 μs , (b) 2.4 μs , (c) and 2.8 μs . In each panel, rephasings are observed at time $\sim 2\tau$. The horizontal arrows indicate the value of τ for each time trace.

where k is the Boltzmann constant and T is the temperature. For the 34.13p–33.67s transition at 295 K, $\gamma_{\text{bb},1} = 5$ kHz. As for mechanism (2), the blackbody field depopulates each Rydberg state at an approximate rate of

$$\gamma_{\text{bb},2} = \frac{4\alpha^3 kT}{3\hbar(n^*)^2}, \quad (5)$$

where α is the fine structure constant. For states with $n^* \approx 34$, $\gamma_{\text{bb},2} \approx 17$ kHz. Both levels undergo this loss of population. The contribution from $\gamma_{\text{bb},1}$ in Eq. (4), however, is implicitly present in Eq. (5). To avoid counting $\gamma_{\text{bb},1}$ twice, we estimate the total contribution of blackbody radiation to the homogeneous decay to be $\gamma_{\text{bb}} = 2\gamma_{\text{bb},2} - \gamma_{\text{bb},1}$, which gives $\gamma_{\text{bb}}^{-1} = 34 \mu\text{s}$. As is the case for the transit time, the blackbody dephasing time is significantly longer than the observed 4.6 μs homogeneous decay time.

The large dipole moments of Rydberg–Rydberg transitions also dephase each other at long range, and the expected homogeneous dephasing rate from the dipole–dipole interaction is⁶³

$$\gamma_{\text{dd}} = \frac{\pi\mu^2 N}{4\epsilon_0 \hbar}. \quad (6)$$

Here, N is the number density of Rydberg states. By comparison, the superradiant decay rate^{51,52} is

$$\gamma_{\text{SR}} = \frac{\pi\mu^2 N L}{3\epsilon_0 \hbar \lambda}, \quad (7)$$

where λ is the wavelength of the radiation, and L is the path length of radiation through the sample. The expression for the superradiant decay rate is substantially similar to that for the dipole–dipole dephasing, except for an additional factor of $\sim L/\lambda$. In our experimental geometry, this factor is large because L is at least 7 cm ($\approx 18\lambda$ for the 34.13p–33.67s transition). Thus, the superradiant decay is expected to be more than 20 times faster than the dipole–dipole dephasing, and we conclude that the dipole–dipole interaction does not contribute significantly to the observed homogeneous decay. On the other hand, if we assume that the observed 4.6 μs homogeneous decay time is entirely due to cooperative effects, Eq. (7) gives a corresponding Rydberg number density of $N = 8 \times 10^4/\text{cm}^3$, which is consistent with previous determinations of the number density in our apparatus.¹⁹ Hence, we conclude that the homogeneous decay in Figs. 6 and 7 is primarily due to superradiance.

IV. CONCLUSIONS AND FUTURE WORK

We have demonstrated broadband, high-resolution, direct detection of Rydberg–Rydberg transitions with CPmmW spectroscopy. Because of the ~ 5 kD transition dipole moments, $\sim 1 \mu\text{W}$ of power for $\sim 1 \mu\text{s}$ is needed to fully polarize a ~ 10 GHz bandwidth, all transitions within which may be detected in each shot with a resolution of ~ 100 kHz. Fast survey acquisition, combined with phase information from the time-domain signals, which distinguishes upward from downward transitions, makes the CPmmW technique well suited to rapid mapping out of manifolds of Rydberg levels.

Additionally, the CPmmW technique provides time-domain observation of dynamical phenomena, such as transient nutations, that are driven by the strong interaction of large transition dipole moments with electromagnetic radiation. Furthermore, Rydberg states may be manipulated by the easily controlled mm-wave source, and the results of these manipulations may be directly monitored with the CPmmW spectrometer. It is possible to sequentially populate states with high angular momentum and determine homogeneous lifetimes. Methods such as adiabatic sweeps^{64,65} and composite pulse sequences^{66,67} should allow for more intricate manipulations. We also probe a cooperative effect, superradiance, using photon echoes. Since the cooperative effects scale linearly with the number density of Rydberg states, a higher density source will allow for a more systematic investigation of these effects. Construction is underway of a collisional cooling photoablation beam source, which will achieve both a higher number density of $\sim 10^8$ particles/cm³ and a narrower Doppler width of ~ 50 kHz.^{68–70} This source will be used for studies of both atomic and molecular systems. Additionally, for the strongest, $|\Delta n^*| \leq 1$ transitions, the μ^2 in Eq. (7) scales as $(n^*)^4$, while the λ^{-1} scales as $(n^*)^{-3}$. So overall, the superradiant decay rate γ_{SR} scales linearly with n^* . Thus, the strength of the cooperative effects may be tuned by varying n^* . One application of the superradiance observations will be a study of the collective Lamb shift.⁷¹

For *molecules* in core-nonpenetrating states ($\ell > 3$), each rovibrational state of the ion-core has its own separate manifold of Rydberg levels because the nonpenetrating Rydberg electron does not interact strongly with the ion-core,¹⁴ which has a vibrational quantum number, v^+ , and a total angular momentum quantum number (exclusive of spin), N^+ . Thus, CPmmW spectra of these states should be simple in that they are “atom-like,” and the molecular spectra would be “pure electronic spectra,” decoupled from the vibrational and rotational motions of the ion-core. These $\Delta v^+ = 0$ and $\Delta N^+ = 0$ selection rules will render the spectra to be trivially assignable, in contrast to assignment of laser transitions, which do not obey such restrictive rotation-vibration selection rules. There will be exclusively $\Delta v^+ = 0$, $\Delta N^+ = 0$ transitions, but the quantum defects will be slightly v^+ , N^+ dependent. This v^+ , N^+ dependence, sampled via CPmmW spectra from selectively laser populated levels with different v^+ , N^+ quantum numbers, reveals the multipole moments and polarizabilities of the ion-core. The CPmmW method offers broadband search capability at sufficient resolution⁷² to determine the multipole moments and polarizabilities of molecular ions through pure electronic spectroscopy of Rydberg molecules. Also, information about weak ℓ , v^+ , N^+ state-mixing may be garnered from the capability to record the $\sim 1\%$ accurate relative intensities inherent in the chirped pulse method.^{15–17} While many molecules in core-penetrating Rydberg states undergo predissociation or autoionization faster than the ~ 1 μ s required for the collection of FID, nonpenetrating ($\ell > 3$) states typically have lifetimes longer than 10 μ s, and so will live long enough to permit the recording of FID spectra. Core-nonpenetrating states of molecules could be populated, for example, by Stark mixing in high- ℓ character with a programmed electric field or by sequentially populating high- ℓ states with a sequence

of short, crafted π pulses. Additionally, BaF is a rare example of a molecule for which the dissociation limit lies above the ionization limit into the lowest electronic state of the ion-core.²⁶ Hence, Rydberg–Rydberg transitions in BaF will be a direct *molecular* application of all of the CPmmW techniques described here.

ACKNOWLEDGMENTS

The authors thank B. H. Pate, J. L. Neill, and G. B. Park for guidance and support regarding the CPmmW spectrometer. The authors also thank D. D. Grimes for his assistance. This work was supported by the National Science Foundation (Grant No. CHE-105879).

¹The effective principal quantum number, n^* , is defined as $n^* \equiv \sqrt{\frac{R}{I-E}}$ = $n - \delta$, where R is the Rydberg constant, I is the ionization limit, E is the energy of the state, n is the principal quantum number, and δ is the quantum defect.

²T. F. Gallagher, *Rydberg Atoms* (Cambridge University Press, Cambridge, 1994).

³H. Lefebvre-Brion and R. W. Field, *The Spectra and Dynamics of Diatomic Molecules* (Elsevier Academic, 2004), p. 352.

⁴C. Fabre, S. Haroche, and P. Goy, *Phys. Rev. A* **18**, 229 (1978).

⁵L. Moi, C. Fabre, P. Goy, M. Gross, S. Haroche, P. Encrenaz, G. Beaudin, and B. Lazareff, *Opt. Commun.* **33**, 47 (1980).

⁶P. Goy, J. M. Raimond, G. Vitrant, and S. Haroche, *Phys. Rev. A* **26**, 2733 (1982).

⁷T. R. Gentile, B. J. Hughey, D. Kleppner, and T. W. Ducas, *Phys. Rev. A* **42**, 440 (1990).

⁸F. Merkt and H. Schmutz, *J. Chem. Phys.* **108**, 10033 (1998).

⁹W. Li, I. Mourachko, M. W. Noel, and T. F. Gallagher, *Phys. Rev. A* **67**, 052502 (2003).

¹⁰F. Merkt and A. Osterwalder, *Int. Rev. Phys. Chem.* **21**, 385 (2002).

¹¹A. Osterwalder, R. Seiler, and F. Merkt, *J. Chem. Phys.* **113**, 7939 (2000).

¹²A. Osterwalder, S. Willitsch, and F. Merkt, *J. Mol. Struct.* **599**, 163 (2001).

¹³A. Osterwalder, A. Wüest, F. Merkt, and C. Jungen, *J. Chem. Phys.* **121**, 11810 (2004).

¹⁴S. R. Lundeen, in *Advances in Atomic, Molecular, and Optical Physics*, edited by P. R. Berman, and C. C. Lin (Elsevier Academic, Amsterdam, 2005), Vol. 52, pp. 161–208.

¹⁵G. G. Brown, B. C. Dian, K. O. Douglass, S. M. Geyer, S. T. Shipman, and B. H. Pate, *Rev. Sci. Instrum.* **79**, 053103 (2008).

¹⁶G. G. Brown, B. C. Dian, K. O. Douglass, S. M. Geyer, and B. H. Pate, *J. Mol. Spectrosc.* **238**, 200 (2006).

¹⁷B. C. Dian, G. G. Brown, K. O. Douglass, and B. H. Pate, *Science* **320**, 924 (2008).

¹⁸G. B. Park, A. H. Steeves, K. Kuyanov-Prozument, J. L. Neill, and R. W. Field, *J. Chem. Phys.* **135**, 024202 (2011).

¹⁹K. Prozument, A. P. Colombo, Y. Zhou, G. B. Park, V. S. Petrović, S. L. Coy, and R. W. Field, *Phys. Rev. Lett.* **107**, 143001 (2011).

²⁰K. Müller-Dethlefs and E. W. Schlag, *Annu. Rev. Phys. Chem.* **42**, 109 (1991).

²¹F. Merkt, *Annu. Rev. Phys. Chem.* **48**, 675 (1997).

²²F. X. Campos, Y. Jiang, and E. R. Grant, *J. Chem. Phys.* **93**, 2308 (1990).

²³A. M. Lyrra, W. T. Luh, L. Li, H. Wang, and W. C. Stwalley, *J. Chem. Phys.* **92**, 43 (1990).

²⁴S. Guizard, N. Shafizadeh, M. Horani, and D. Gauyacq, *J. Chem. Phys.* **94**, 7046 (1991).

²⁵S. T. Pratt, J. L. Dehmer, P. M. Dehmer, and W. A. Chupka, *J. Chem. Phys.* **101**, 882 (1994).

²⁶Z. J. Jakubek and R. W. Field, *Phys. Rev. Lett.* **72**, 2167 (1994).

²⁷K. Siglow, R. Neuhauser, and H. J. Neusser, *J. Chem. Phys.* **110**, 5589 (1999).

²⁸P. Bell, F. Aguirre, E. R. Grant, and S. T. Pratt, *J. Chem. Phys.* **119**, 10146 (2003).

²⁹J. J. Kay, D. S. Byun, J. O. Clevenger, X. Jiang, V. S. Petrović, R. Seiler, J. R. Barchi, A. J. Merer, and R. W. Field, *Can. J. Chem.* **82**, 791 (2004).

- ³⁰K. Afrousheh, P. Bohlouli-Zanjani, D. Vagale, A. Mugford, M. Fedorov, and J. D. D. Martin, *Phys. Rev. Lett.* **93**, 233001 (2004).
- ³¹S. T. Pratt, *Annu. Rev. Phys. Chem.* **56**, 281 (2005).
- ³²T. Wang, S. F. Yelin, R. Côté, E. E. Eyler, S. M. Farooqi, P. L. Gould, M. Kořtrun, D. Tong, and D. Vrinceanu, *Phys. Rev. A* **75**, 33802 (2007).
- ³³N. J. A. Jones, R. S. Minns, R. Patel, and H. H. Fielding, *J. Phys. B* **41**, 185102 (2008).
- ³⁴H. Park, P. J. Tanner, B. J. Claessens, E. S. Shuman, and T. F. Gallagher, *Phys. Rev. A* **84**, 22704 (2011).
- ³⁵S. D. Hogan, J. A. Agner, F. Merkt, T. Thiele, S. Filipp, and A. Wallraff, *Phys. Rev. Lett.* **108**, 063004 (2012).
- ³⁶Reference 5, where superradiant emission of a sodium transition in a cavity was heterodyne-detected, is one example.
- ³⁷J. Sugar and C. Corliss, *J. Phys. Chem. Ref. Data* **14**, 1 (1985).
- ³⁸W. R. S. Garton and K. Codling, *Proc. Phys. Soc.* **86**, 1067 (1965).
- ³⁹C. M. Brown, S. G. Tilford, and M. L. Ginter, *J. Opt. Soc. Am.* **63**, 1454 (1973).
- ⁴⁰J. A. Armstrong, P. Esherick, and J. J. Wynne, *Phys. Rev. A* **15**, 180 (1977).
- ⁴¹S. A. Borgström and J. R. Rubbmark, *J. Phys. B* **10**, 3607 (1977).
- ⁴²A. G. Vaidyanathan, W. P. Spencer, J. R. Rubbmark, H. Kuiper, C. Fabre, D. Kleppner, and T. W. Ducas, *Phys. Rev. A* **26**, 3346 (1982).
- ⁴³The paperback version of Ref. 3 serves as a 25-dB attenuator from 70 to 84 GHz.
- ⁴⁴T. F. Gallagher and P. Pillet, in *Advances in Atomic, Molecular, and Optical Physics*, edited by E. Arimondo, P. R. Berman, and C. C. Lin (Elsevier Academic, Amsterdam, 2008), Vol. 56, pp. 161–218.
- ⁴⁵J. M. Raimond, G. Vitrant, and S. Haroche, *J. Phys. B* **14**, L655 (1981).
- ⁴⁶W. R. Anderson, J. R. Veale, and T. F. Gallagher, *Phys. Rev. Lett.* **80**, 249 (1998).
- ⁴⁷I. Mourachko, D. Comparat, F. de Tomasi, A. Fioretti, P. Nosbaum, V. M. Akulin, and P. Pillet, *Phys. Rev. Lett.* **80**, 253 (1998).
- ⁴⁸J. Stanojevic, R. Côté, D. Tong, E. E. Eyler, and P. L. Gould, *Phys. Rev. A* **78**, 052709 (2008).
- ⁴⁹P. J. Tanner, J. Han, E. S. Shuman, and T. F. Gallagher, *Phys. Rev. Lett.* **100**, 043002 (2008).
- ⁵⁰R. H. Dicke, *Phys. Rev.* **93**, 99 (1954).
- ⁵¹N. Skribanowitz, I. P. Herman, J. C. MacGillivray, and M. S. Feld, *Phys. Rev. Lett.* **30**, 309 (1973).
- ⁵²J. C. MacGillivray and M. S. Feld, *Phys. Rev. A* **14**, 1169 (1976).
- ⁵³F. Gounand, M. Hugon, P. R. Fournier, and J. Berlande, *J. Phys. B* **12**, 547 (1979).
- ⁵⁴M. Gross, P. Goy, C. Fabre, S. Haroche, and J. M. Raimond, *Phys. Rev. Lett.* **43**, 343 (1979).
- ⁵⁵Y. Zhou, *Mol. Phys.* **110**, 1909 (2012).
- ⁵⁶For values of the Rydberg constant and the ionization limit that may be used to compute n^* in calcium, see, for example, Ref. 7.
- ⁵⁷J. C. McGurk, T. G. Schmalz, and W. H. Flygare, *J. Chem. Phys.* **60**, 4181 (1974).
- ⁵⁸H. C. Torrey, *Phys. Rev.* **76**, 1059 (1949).
- ⁵⁹J. C. McGurk, R. T. Hofmann, and W. H. Flygare, *J. Chem. Phys.* **60**, 2922 (1974).
- ⁶⁰D. W. Posener, *J. Magn. Reson.* **14**, 121 (1974).
- ⁶¹L. Chen, C. E. Cottrell, and A. G. Marshall, *Chemom. Intell. Lab. Syst.* **1**, 51 (1986).
- ⁶²For a linearly chirped excitation, the nonresonant contributions to the phase above and below the resonance frequency cancel, and the phase of the excitation at the resonance frequency determines the phase of the FID.
- ⁶³V. M. Akulin and N. V. Karlov, *Intense Resonant Interactions in Quantum Electronics*, Texts and Monographs in Physics (Springer-Verlag, Berlin, 1992).
- ⁶⁴Ě. Kupče and R. Freeman, *J. Magn. Reson., Ser. A* **117**, 246 (1995).
- ⁶⁵J. Baum, R. Tycko, and A. Pines, *Phys. Rev. A* **32**, 3435 (1985).
- ⁶⁶M. H. Levitt and R. Freeman, *J. Magn. Reson.* **33**, 473 (1979).
- ⁶⁷R. Freeman, S. P. Kempell, and M. H. Levitt, *J. Magn. Reson.* **38**, 453 (1980).
- ⁶⁸J. K. Messer and F. C. De Lucia, *Phys. Rev. Lett.* **53**, 2555 (1984).
- ⁶⁹S. E. Maxwell, N. Brahms, R. deCarvalho, D. R. Glenn, J. S. Helton, S. V. Nguyen, D. Patterson, J. Petricka, D. DeMille, and J. M. Doyle, *Phys. Rev. Lett.* **95**, 173201 (2005).
- ⁷⁰D. Patterson and J. M. Doyle, *J. Chem. Phys.* **126**, 154307 (2007).
- ⁷¹M. O. Scully and A. A. Svidzinsky, *Science* **328**, 1239 (2010).
- ⁷²J. J. Kay, S. L. Coy, V. S. Petrović, B. M. Wong, and R. W. Field, *J. Chem. Phys.* **128**, 194301 (2008).